Check for updates

OPEN

Coexistence of valley polarization and Chern insulating states in MoS$_2$ monolayers with n-p codoping

Xinyuan Wei[1], Jiayong Zhang[2,1], Bao Zhao[1,3] & Zhongqin Yang[1,4] ✉

The electronic and topological properties of MoS$_2$ monolayers with n-p codoping effect are investigated by using first-principles calculations. Two types of the doped Nb atoms play the roles of the p-type and n-type dopants, respectively. The n-p codoping is found inducing a large valley polarization, associated with the strong magnetization induced by the Nb dopants. Interestingly, the system simultaneously owns a perfect Chern insulating band gap opened exactly at the Fermi level. The nontrivial band gap comes from the lifting of the degeneracy of the d$_{xz}$ and d$_{yz}$ orbitals of Nb$_2$ atoms after the spin-orbit coupling is considered. Our work inspires exciting prospects to tune the novel properties of materials with n-p codoping effects.

Recently, transition-metal dichalcogenides (TMDs) have been proposed as excellent candidates for electronics, spintronics, and valleytronics materials by manipulating the charge, spin, and valley degrees of freedom in the system[1–4]. For example, the experimental realization of valley polarization could be through optical pumping[5,6] in MoS$_2$ monolayers (MLs) or externally applied magnetic fields[7–9] in WSe$_2$ and MoSe$_2$ monolayers. The approach of optical pumping is, however, restricted by the limited carrier lifetimes in dynamical process. And the valley polarization achieved through an external magnetic field is generally quite small. An alternative way to control the valley degree of freedom in TMDs is through magnetic atom doping[10,11] or the proximate effect from magnetic substrates[12].

N-p codoping, with both n-type and p-type dopants in one material, has been proved to be an effective strategy to tune the electronic properties[13–15]. Ferromagnetic (FM) order was reported in graphene with Ni-B codoping[13]. And quantum anomalous Hall effect was predicted in graphene[14] and Sb$_2$Te$_3$[15] through n-p codoping. In this work, we explore the electronic structures and valleytronics in the MoS$_2$ monolayer with n-p codoping. Very large valley polarization at the MoS$_2$ valence bands is obtained, attributed to the imbalance of K and K′ bands aroused by the magnetic Nb dopants. Chern insulating states are also found in the system. The coexistence of valley polarization and Chern insulating effects in the MoS$_2$ ML with Nb n-p codoping demonstrates that this kind of system has potential applications in not only valleytronics, but also electronics and spintronics, which will greatly facilitate the device integration in practice.

Results and discussion

For the 3×3 supercell MoS$_2$ ML with one Mo substituted by Nb atom (Nb$_1$), the Nb tends to substitute the Mo atom instead of the S atom for both rich Mo and S cases, consistent with the tendency reported in previous researches[16–20]. The Nb$_1$ substituted MoS$_2$ ML is also proved to be dynamically stable (without imaginary frequency) through the density functional perturbation theory (DFPT)[21]. Based on this structure, four typical high-symmetry adsorption sites are considered for Nb$_2$ atom, with the adsorption energy calculated as: $E_a = E_{sample} + E_{adatom} - E_{total}$. The E_{sample}, E_{adatom}, and E_{total} are the total energies of the MoS$_2$ ML with Nb$_1$ doping, the single Nb atom, the MoS$_2$ ML with Nb$_1$-Nb$_2$ codoping, respectively. As shown in Table 1, the most stable configuration is N (see Fig. 1(a)). For comparison, the obtained adsorption energy of the most stable configuration M for the pristine MoS$_2$ ML with Nb$_2$ adsorption is also given in Table 1. As the definition indicates, the

[1]State Key Laboratory of Surface Physics and Key Laboratory of Computational Physical Sciences (MOE) & Department of Physics, Fudan University, Shanghai, 200433, China. [2]Jiangsu Key Laboratory of Micro and Nano Heat Fluid Flow Technology and Energy Application, School of Mathematics and Physics, Suzhou University of Science and Technology, Suzhou, Jiangsu, 215009, China. [3]School of Physics Science and Information Technology, Shandong Key Laboratory of Optical Communication Science and Technology, Liaocheng University, Liaocheng, Shandong, 252059, China. [4]Collaborative Innovation Center of Advanced Microstructures, Fudan University, Shanghai, 200433, China. ✉e-mail: zyang@fudan.edu.cn

1

Doping Type	Site	E_a (eV)	M_T (μ_B)	M_{Nb1} (μ_B)	M_{Nb2} (μ_B)
Nb$_1$-Nb$_2$ codoping	H	3.408	4.00	0.05	2.76
	M	3.750	4.00	0.01	2.44
	N	**3.789**	**4.00**	**0.05**	**2.49**
	S	−0.065	3.80	0.09	2.37
Nb$_2$ doping	**M**	**2.485**	**5.00**	/	**2.53**

**Table 1.** The adsorption energies (E_a), total and local magnetic moments (M_T, M_{Nb1}, M_{Nb2}) in the MoS$_2$ MLs with Nb$_1$-Nb$_2$ codoping or only Nb$_2$ doping. The most stable configurations are marked in bold.
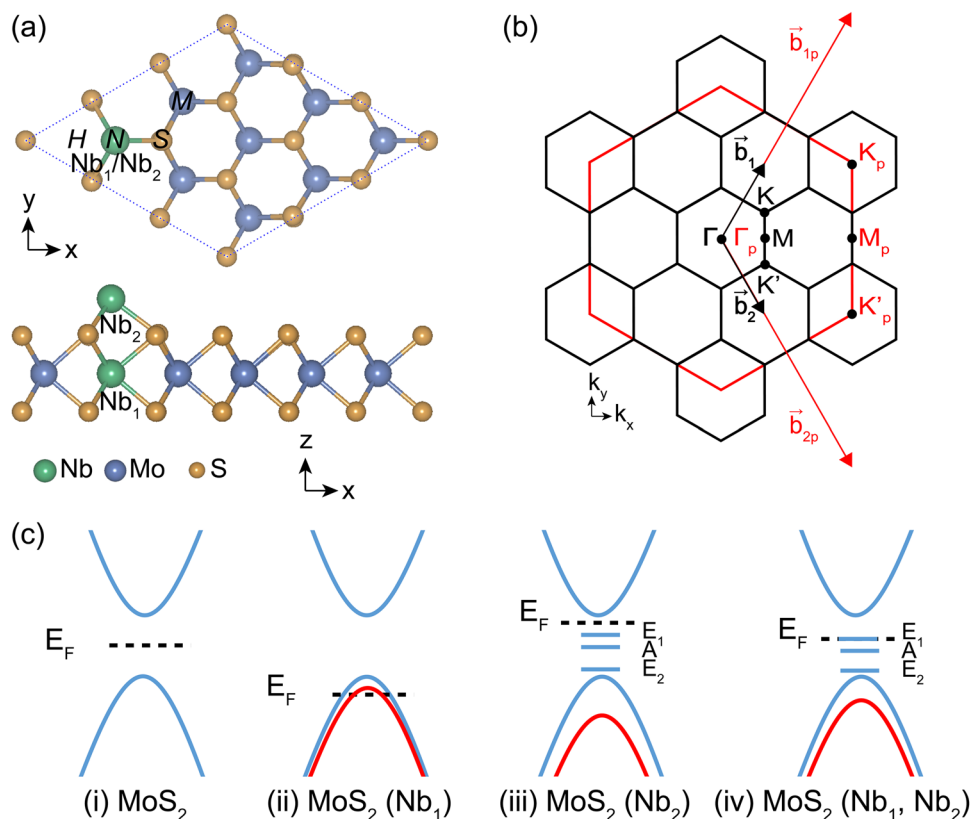
Figure 1. (**a**) Top and side views of the 3×3 supercell of the MoS$_2$ ML with Nb n-p codopants. The side view is for the N configuration. (**b**) Reciprocal momentum space structure, the red and black hexagons/arrows are the reciprocal lattices/vectors for the 1×1 and 3×3 supercells, respectively. The special k-points for the 1×1 supercell are marked with subscript p. (**c**) Evolution of the band structures for the pristine MoS$_2$ ML (i) and the Nb$_1$ doped (ii), Nb$_2$ doped (iii), and Nb$_1$-Nb$_2$ codoped (iv) MoS$_2$ MLs.

adsorption energy reflects the interaction strength between the Nb$_2$ atom and the two-dimensional sheet. For the pristine MoS$_2$ ML, the adsorption energy is 2.485 eV, while if the sheet is the Nb$_1$ doped MoS$_2$ ML (Fig. 1(a)), the adsorption energy increases to 3.789 eV. Thus, we infer that the interaction strength of the Nb$_2$ adatom in the Nb$_1$-Nb$_2$ codoping case is enhanced (by 1.3 eV). This behavior can be ascribed to the strong electrostatic attractive interaction between the n-type (Nb$_2$) and p-type (Nb$_1$) dopants. In the following, we primarily focus on the most stable N configuration for the Nb$_1$-Nb$_2$ codoping case.

The band structure and the densities of states (DOSs) for the MoS$_2$ ML with Nb$_1$-Nb$_2$ codoping are given in Fig. 2(a) and the upper panel of Fig. 2(b), respectively. The spin-orbit coupling (SOC) is not yet considered. The Nb$_1$ DOSs distribute over a wide range of energy, similar to those of Mo atoms in the pristine MoS$_2$[22], indicating strong bonds formed between Nb$_1$ and its neighboring S atoms. The DOSs of the Nb$_2$ are, however, mainly located within the band gap of the pristine MoS$_2$. To further comprehend the roles of the two types of Nb atoms, the electronic structures of the pristine MoS$_2$ ML with solely Nb$_1$ or Nb$_2$ are also calculated. For the MoS$_2$ ML with one Mo atom substituted by one Nb atom in the 3×3 supercell, labeled as MoS$_2$ (Nb$_1$), the Fermi level (E_F) is now located below the top of the valence bands of the pristine MoS$_2$ (middle panel of Fig. 2(b)), implying the p-type acceptor character of Nb$_1$ dopant. When one Nb atom is adsorbed on the top of one of the Mo atoms of the pristine MoS$_2$ ML, marked as MoS$_2$ (Nb$_2$), the E_F of the system is very close to the bottom of the conduction bands of
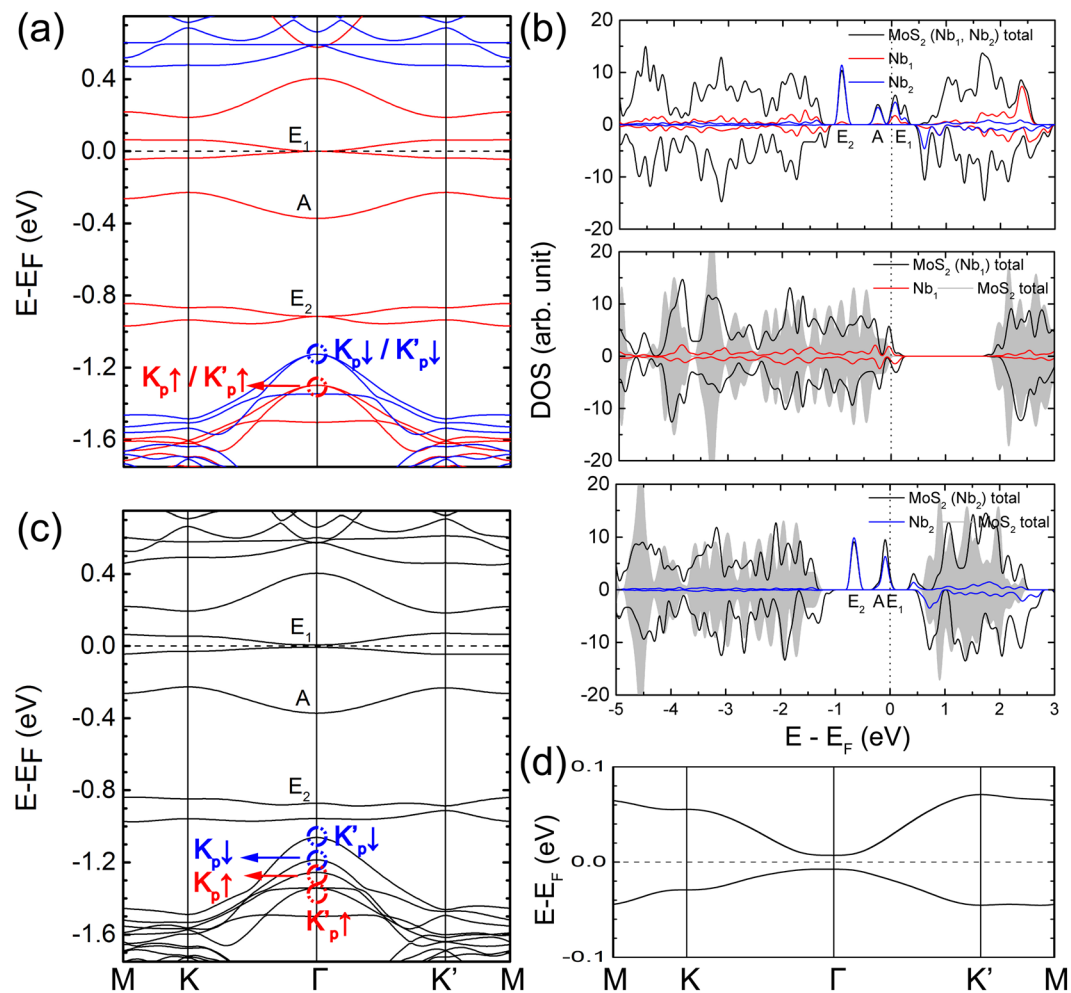
Figure 2. (**a**) Band structure of the Nb_1-Nb_2 codoped MoS_2 ML without SOC. The red and blue curves show the spin-up and spin-down components, respectively. The black curves in the upper, middle, and lower panels of (**b**) are the total DOSs of the Nb_1-Nb_2 codoped, Nb_1 doped, and Nb_2 doped MoS_2 MLs, respectively. The red/blue curves are the partial DOSs of the Nb_1/Nb_2 atom. The gray areas in the middle and lower panels of (**b**) are the total DOSs of the pristine MoS_2 ML. The Nb_1 and Nb_2 partial DOSs are quadrupled and doubled to obtain a clear view. The positive and negative values correspond to the spin-up and spin-down components, respectively. (**c,d**) are the normal and enlarged views of the band structures of the Nb_1-Nb_2 codoped MoS_2 ML with SOC. The small red/blue circles in (**a,c**) indicate the spin-up/spin-down component located around Γ, folded from the K_p and K'_p in the primitive cell.

the pristine MoS_2 (lower panel of Fig. 2(b)). Thus, Nb_2 adatom acts as the n-type donor. The *d* orbital of Nb_2 atom splits into A (d_{z2}), E_1 (d_{xz}, d_{yz}), and E_2 (d_{xy}, $d_{x2−y2}$) (Fig. 2(a,b)), due to the C_{3v} symmetry owned.

The band evolution from the pristine MoS_2 ML to the Nb_1-Nb_2 codoped MoS_2 ML is summarized in Fig. 1(c). For the pristine MoS_2 ML, the E_F is within the band gap. For the MoS_2 (Nb_1) case, the E_F moves downwards to the valence bands of the pristine MoS_2, while for the MoS_2 (Nb_2) case, the E_F moves upper to the conduction bands of the pristine MoS_2, indicating Nb_1 and Nb_2 act as p-type and n-type dopants, respectively. For the MoS_2 (Nb_1, Nb_2) case, the compensation effect of the n-type and p-type doping causes the E_F located exactly at the E_1 bands.

Besides the movements of the E_F position, the magnetic behaviors of the Nb_1 and Nb_2 atoms in the systems are also different from each other. For example, the MoS_2 (Nb_1) is weakly spin polarized with a total magnetic moment of 0.73 μB (the middle panel in Fig. 2(b)), while the total magnetic moment is 5.00 μB for the MoS_2 (Nb_2). The strong magnetism of the MoS_2 (Nb_2) can be comprehended through strong atomic behavior of Nb_2 atoms, consistent with the case of the *3d* transition metal atom adsorption in MoS_2 MLs in previous studies[23,24]. For the Nb n-p codoping case, the total magnetic moment of 4.00 μB, instead of 5.00 μB, is obtained for the most stable *N* configuration. The decrease of the magnetism in the n-p codoping case can be ascribed to the p-type Nb_1 in the n-p codoping case gaining one unpaired electron from Nb_2. The local magnetic moments of the Nb_1 and Nb_2 in the n-p codoped system are about 0.05 μB and 2.49 μB, respectively. Thus, the magnetism in the n-p codoped MoS_2 ML is primarily induced by the Nb_2 adatoms. To find whether the above FM structure is the magnetic ground state, the total energies of non-magnetic (NM) and antiferromagnetic (AFM) structures are also calculated. The total energy of the FM ordering per Nb_1-Nb_2 pair is found to be lower than that of the NM ordering
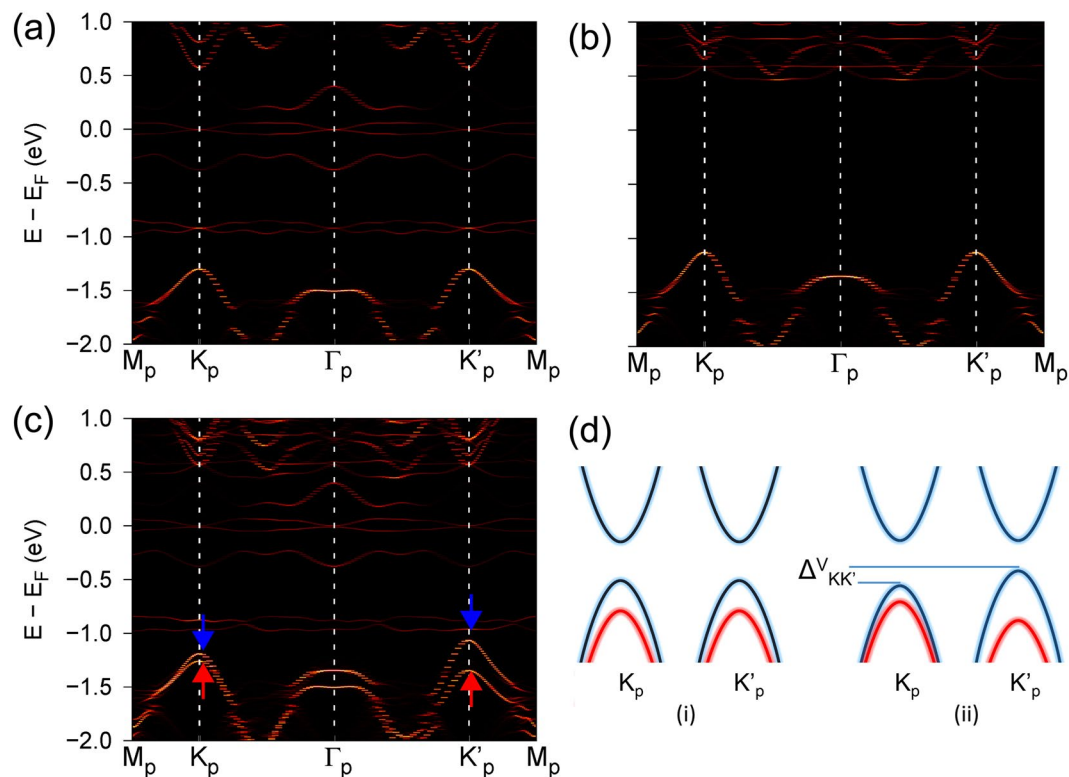
Figure 3. Unfolded band structures for the Nb n-p codoped MoS_2 ML. (**a**,**b**) are for the spin-up and spin-down bands without SOC, respectively. (**c**) is for the SOC calculation. The small red/blue arrow indicates the spin-up/spin-down bands. (**d**) Schematic diagrams of the bands around the K_p and K'_p points without (i) and with (ii) SOC in the primitive cell. The red and blue curves represent the bands with different spin components.

by 355 meV and AFM ordering by 2 meV. Thus, the FM ordering is the most stable magnetic configuration for the Nb codoped system. The Curie temperature (T_c) estimated with the mean-field approximation[25] is about 15.5 K.

The C_{3v} symmetry owned by the system makes the E_1 (d_{xz}, d_{yz}) and E_2 (d_{xy}, d_{x2-y2}) bands both be degenerate at the Γ point with quadratic non-Dirac band dispersions before the SOC is included (Fig. 2(a)). Under this case, the system could be called as a spin-gapless semiconductor (SGS)[26–28] for the bands at the E_F are 100% spin polarized. When the SOC is included, the doubly degenerate energy points at the Γ point are lifted and band gaps are opened, as shown in Fig. 2(c,d). Additionally, the degeneracy of the tops of the valence bands of the pristine MoS_2 (around -1.2 eV in Fig. 2(a)) is also lifted (Fig. 2(c)). E_1 is exactly located at the E_F without the SOC (Fig. 2(a)) and a global band gap of 15.0 meV is opened by the SOC in the system (Fig. 2(d)). We also check the results by using the HSE06 functional[29]. The calculations show that the main feature keeps undistributed with the HSE06 functional, i.e., the E_1 bands are still located around the E_F and a global band gap is also opened. The opened band gap is 36.4 meV, larger than the result obtained from the metaGGA method, due to the stronger exchange-correlation interactions predicted for the Nb d_{xz} and d_{yz} orbitals in the HSE06 functional. The real value of the band gap may be determined by future experimental measurements. Hence, the n-p codoped MoS_2 ML is an insulator. As shown in Fig. 1(c), if there is no Nb_1 in the system, the E_1 bands are totally occupied by electrons. It is, thus, the Nb n-p codoping that gives rise to the E_1 bands located exactly at the E_F.

Due to the strong magnetism of the Nb_2 adatoms, legible spin polarization of about 0.2 eV is induced at the tops of the valence bands of MoS_2 (around -1.2 eV in Fig. 2(a)). This magnetism together with the broken space-inversion symmetry in the system may lead to valley polarization effect[30,31]. However, the use of the 3×3 supercell in the calculations causes band folding. To explore the valley polarization of the n-p codoped MoS_2 ML, the bands shown in Fig. 2(a,c) are unfolded onto the k-points in the Brillouin zone (BZ) of the 1×1 primitive cell (Fig. 1(b)) by using a k-projection method[32–34]. Figure 3(a,b) show the unfolded bands for the Nb n-p codoped MoS_2 ML without SOC. The obvious spin polarization in the valence bands of the MoS_2 is also outstanding. The bands at K_p and K'_p for both the spin-up and spin-down components are degenerate, whose sketches are displayed in the (i) case of Fig. 3(d). Thus, no valley polarization appears in the bands.

When the SOC is included, a valley polarization of 125 meV can be observed, defined as $\Delta V_{KK'} = E^V_{K'_p} - E^V_{K_p}$. When the HSE06 functional is employed, an almost same value of the valley polarization is obtained, due to the small exchange-correlation interaction for the Mo d orbitals mainly contributing to the valley bands in the system. Only in the unfolded bands (Fig. 3(c)), the valley polarization can be distinguished. How the tops of the valence bands of the MoS_2 in Fig. 2(c) correspond to the K_p or K'_p points in the MoS_2 primitive cell is also illustrated. Figure 3(d) shows the schematic diagrams of the valley polarization formed in the Nb n-p codoped MoS_2 ML. Reference[12] has found that the magnitude of the valley polarization is limited by the smaller spin splitting
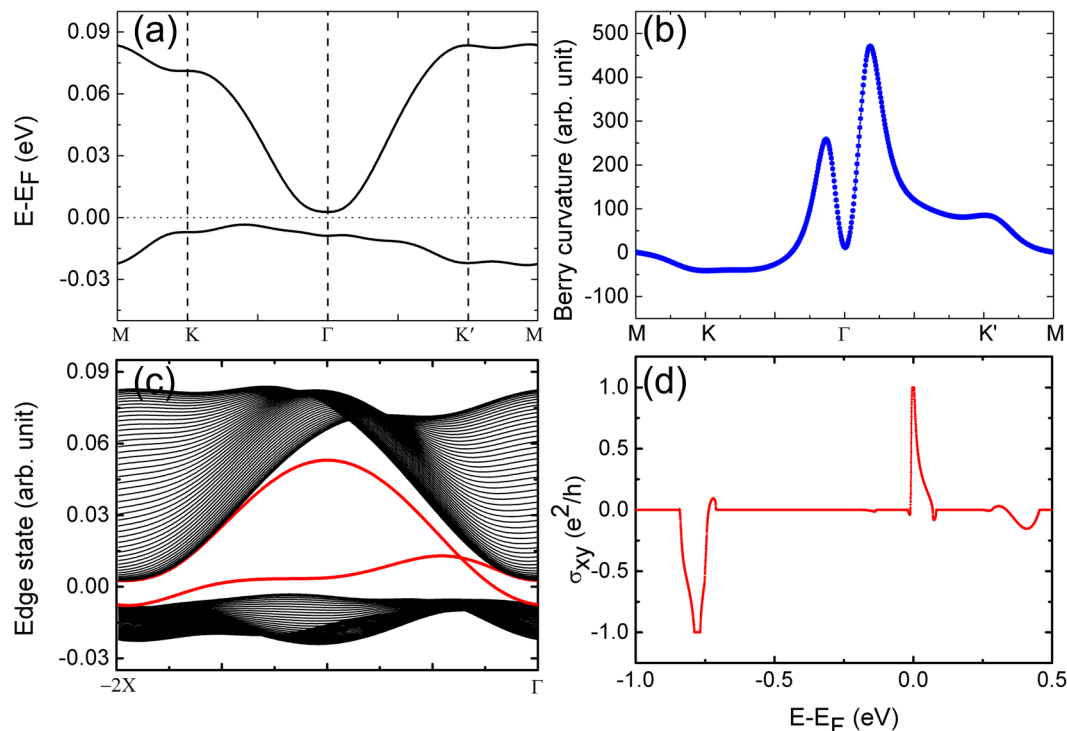
Figure 4. Wannier-function fitted bands around the E_F (**a**), Berry curvatures (**b**), edge states (**c**), and Hall conductivity (**d**) for the Nb_1-Nb_2 codoped MoS_2 ML.

arising from the SOC or the exchange field. Therefore, the valley polarization obtained (125 meV) should be limited by the smaller SOC strength other than the spin polarization (200 meV). The valley polarization may be enhanced further with the increase of the SOC, by such as substituting the atoms with heavier elements. The obtained valley polarization is actually an intrinsic attribute owned by the system and no magnetic field or optical pumping is necessary to realize the effect. This valley polarization makes the Nb n-p codoped MoS_2 ML can be called as a ferrovalley material. If the spin orientations of the Nb atoms are reversed, the band features at K and K′ are exchanged, similar to the case in ref. [35]. Thus, the ferrovalley property still exists in the system, with the same valley polarization strength, but an opposite sign. Since the total energies of the two systems are the same, the two ferrovalley states can be regarded as energy degenerate states.

We now identify the possible topological behaviors of the band gap opened at the E_F (Fig. 2(d)). The bands are fitted by using maximally localized Wannier functions (MLWFs) method[36–38] (Fig. 4(a)). The Berry curvatures can then be calculated. Two peaks of the Berry curvatures appear around the Γ point (Fig. 4(b)), ascribed to the parabolic band dispersions of E_1 (Fig. 2(a)) without SOC[39]. The calculated Chern number of 1 gives a direct evidence for the existence of Chern insulating state in the system. Figure 4(c) displays the band structure of a one-dimensional Nb n-p codoped MoS_2 nanoribbon, calculated by using the tight-binding model constructed from the MLWFs. The two edge states (red curves in Fig. 4(c)) connecting the conduction and valence bands exist inside the SOC induced band gap, representing one chiral dissipationless conducting channel existing on each side of the nanoribbon sample. Besides, the edge states should be 100% spin-polarized and half-metallic since the two-fold E_1 bands in Fig. 2(a) are spin up[40,41], availing the applications of the Nb n-p codoped MoS_2 ML system in spintronic devices. The quantized Hall conductivity of e^2/h at E_F (Fig. 4(d)) matches well with the nontrivial band gap contributed by E_1 orbitals, while the Hall conductivity of $-e^2/h$ at -0.8 eV appears due to the E_2 orbitals. The forming mechanism of these topological states can be ascribed to the SOC-induced band splitting of the degenerate quadratic non-Dirac bands at the Γ point[39–41]. Thus, the large ferrovalley effect and the Chern insulating state achieved in the Nb n-p codoped MoS_2 monolayer are contributed from the bands at the K (K′) and Γ points in the momentum space, respectively.

The electronic and topological properties of the Nb codoped systems with different Nb doping concentrations are also studied. If the Nb doping concentration is increased, such as one pair of Nb_1-Nb_2 doped in one 2×2 supercell, the band structure is found being changed much and becomes metallic, ascribed to the strong interaction between the different Nb pairs. If the Nb doping concentration is lowered, for example, one pair of Nb_1-Nb_2 doped in one 4×4 supercell, the valley polarization and the nontrivial bands can still be clearly observed, although global band gaps may not be opened. Therefore, the Nb doping concentration should be carefully examined to give perfect Chern insulting states and large valley polarization in the MoS_2 MLs.

In experiments, the n-p codoping has been realized in some materials, such as dilute magnetic semiconductors of ZnMnAlO and ZnCoAlO[42]. Based on these techniques, the n-p codoped MoS_2 ML may be fabricated by following two steps. First, synthesize the p-type doped MoS_2 ML with Nb_1 atoms substituting the Mo atoms via e-beam evaporation plus chemical vapor deposition (CVD), as implemented in ref. [16] or chemical vapor transport

(CVT) in refs. [17],[18]. Second, deposit some Nb atoms onto the surface of the prepared p-type MoS_2 ML. Due to the electrostatic attraction between the n-type and p-type dopants, these deposited Nb atoms (Nb_2) tend to be located on the top of the Nb_1 atoms, as the obtained adsorption energies indicate. In this way, the Nb n-p codoped system might be achieved in experiments.

Conclusion

The electronic states of the Nb n-p codoped MoS_2 monolayer are studied with *ab initio* calculations. Two Nb atoms (Nb_1 and Nb_2) serve as p-type and n-type dopants, respectively. Large valley polarization is predicted, caused by the induced magnetism together with the broken space-inversion symmetry and the SOC interaction in the MoS_2 system. The Nb n-p codoped MoS_2 monolayer is also a Chern insulator, whose edge can conduct the pure spin-up current without energy dissipation. The coexistence of the large valley polarization and Chern insulting states provides encouraging routes in applying the codoped two-dimensional materials in the fabrication of valleytronic, microelectronic, and spintronic devices.

Methods

Since experimental studies have shown that the Mo atoms in MoS_2 thin films can be substituted by Nb atoms as efficient acceptors[16–18], we build the MoS_2 ML with n-p codoping by first substituting one of the Mo atoms in the 3×3 supercell with an Nb atom, marked as Nb_1 in Fig. 1(a). Another Nb atom (Nb_2) is then considered to adsorb at the surface of the MoS_2 ML. Totally four typical adsorption sites are explored for the Nb_2 atom: *H* (Hollow), *M* (Mo-top), *N* (Nb_1-top), and *S* (S-top) (Fig. 1(a))[43]. Some other adsorption sites, far away from the Nb_1 atom, are also considered, which are, however, found being unfavorable in energy, compared with the above corresponding sites. The calculations of the electronic structures are performed by using first-principles methods[44]. The exchange-correlation interaction is described with the metaGGA with SCAN form[45]. The energy cutoff is set as 450 eV. Monkhorst-Pack k-point meshes with $5 \times 5 \times 1$ are adopted for structural relaxation and electronic structure calculations. The experimental lattice constant of 3.16 Å[46] is used and the vacuum space along the z direction is set about 20 Å. The test calculations show that the Nb dopants can expand slightly the lattice structure. Since the energy bands are found insensitive to the lattice constant, the experimental lattice is employed in the subsequent calculations. The convergences of the total energy and Hellmann-Feynman forces are set to be 10^{-6} eV and 0.01 eV/Å, respectively.

References

1. Manzeli, S., Ovchinnikov, D., Pasquier, D., Yazyev, O. V. & Kis, A. 2D transition metal dichalcogenides. *Nat. Rev. Mater.* **2**, 17033 (2017).
2. Wei, Z. *et al*. Various structures of 2D transition-metal dichalcogenides and their applications. *Small Methods* **2**, 1800094 (2018).
3. Han, G. H., Duong, D. L., Keum, D. H., Yun, S. J. & Lee, Y. H. van der Waals metallic transition metal dichalcogenides. *Chem. Rev.* **118**, 6297–6336 (2018).
4. Wei, X. Y. *et al*. Chern insulators without band inversion in MoS_2 monolayers with 3d adatoms. *Phys. Rev. B* **95**, 075419 (2017).
5. Mak, K. F., McGill, K. L., Park, J. & McEuen, P. L. The valley Hall effect in MoS_2 transistors. *Science* **344**, 1489 (2014).
6. Zeng, H., Dai, J., Yao, W., Xiao, D. & Cui, X. Valley polarization in MoS_2 monolayers by optical pumping. *Nat. Nanotechnol.* **7**, 490 (2012).
7. Aivazian, G. *et al*. Magnetic control of valley pseudospin in monolayer WSe_2. *Nat. Phys.* **11**, 148 (2015).
8. MacNeill, D. *et al*. Breaking of valley degeneracy by magnetic field in monolayer $MoSe_2$. *Phys. Rev. Lett.* **114**, 037401 (2015).
9. Srivastava, A. *et al*. Valley Zeeman effect in elementary optical excitations of monolayer WSe_2. *Nat. Phys.* **11**, 141–147 (2015).
10. Chen, X., Zhong, L., Li, X. & Qi, J. Valley splitting in the transition-metal dichalcogenide monolayer via atom adsorption. *Nanoscale* **9**, 2188 (2017).
11. Singh, N. & Schwingenschlögl, U. A Route to permanent valley polarization in monolayer MoS_2. *Adv. Mater.* **29**, 1600970 (2017).
12. Li, N. B., Zhang, J. Y., Xue, Y., Zhou, T. & Yang, Z. Q. Large valley polarization in monolayer $MoTe_2$ on a magnetic substrate. *Phys. Chem. Chem. Phys.* **20**, 3805 (2018).
13. Qi, S., Chen, H., Xu, X. & Zhang, Z. Diluted ferromagnetic graphene by compensated n–p codoping. *Carbon* **61**, 609–615 (2013).
14. Deng, X. *et al*. Realization of quantum anomalous Hall effect in graphene from n-p codoping-induced stable atomic adsorption. *Phys. Rev. B* **95**, 121410(R) (2017).
15. Qi, S. *et al*. High-Temperature Quantum anomalous Hall effect in n-p codoped topological insulators. *Phys. Rev. Lett.* **117**, 056804 (2016).
16. Laskar, M. R. *et al*. p-type doping of MoS_2 thin films using Nb. *Appl. Phys. Lett.* **104**, 092104 (2014).
17. Suh, J. *et al*. Reconfiguring crystal and electronic structures of MoS_2 by substitutional doping. *Nat. Commun.* **9**, 199 (2018).
18. Suh, J. *et al*. Doping against the native propensity of MoS_2: degenerate hole doping by cation substitution. *Nano Lett.* **14**, 6976–6982 (2014).
19. Dolui, K., Rungger, I., Das Pemmaraju, C. & Sanvito, S. Possible doping strategies for MoS_2 monolayers: an ab initio study. *Phys. Rev. B* **88**, 075420 (2013).
20. Onofrio, N., Guzman, D. & Strachan, A. Novel doping alternatives for single-layer transition metal dichalcogenides. *J. Appl. Phys.* **122**, 185102 (2017).
21. Togo, A. & Tanaka, I. First principles phonon calculations in materials science. *Scr. Mater.* **108**, 1–5 (2015).
22. Feng, W. X. *et al*. Intrinsic spin Hall effect in monolayers of group-VI dichalcogenides: a first-principles study. *Phys. Rev. B* **86**, 165108 (2012).
23. Wang, Y. *et al*. First-principles study of transition-metal atoms adsorption on MoS_2 monolayer. *Physica E* **63**, 276–282 (2014).
24. Li, X. D., Fang, Y. M., Wu, S. Q. & Zhu, Z. Z. Adsorption of alkali, alkaline-earth, simple and 3d transition metal, and nonmetal atoms on monolayer MoS_2. *AIP Adv.* **5**, 057143 (2015).
25. Shi, H. L., Pan, H., Zhang, Y.-W. & Yakobson, B. I. Strong ferromagnetism in hydrogenated monolayer MoS_2 tuned by strain. *Phys. Rev. B* **88**, 205305 (2013).
26. Wang, X. L. Proposal for a new class of materials: Spin Gapless Semiconductors. *Phys. Rev. Lett.* **100**, 156404 (2008).
27. Wang, X. T., Li, T. Z., Cheng, Z. X., Wang, X.-L. & Chen, H. Recent advances in Dirac spin-gapless semiconductors. *App. Phys. Rev.* **5**, 041103 (2018).

28. Wang, X. T., Cheng, Z. X., Wang, J. L., Wang, X.-L. & Liu, G. D. Recent advances in the Heusler based spin-gapless semiconductors. *J. Mater. Chem. C* **4**, 7176 (2016).
29. Heyd, J., Scuseria, G. E. & Ernzerhof, M. Hybrid functionals based on a screened coulomb potential. *J. Chem. Phys.* **118**, 8207 (2003).
30. Tong, W.-Y., Gong, S.-J., Wan, X. & Duan, C.-G. Concepts of ferrovalley material and anomalous valley Hall effect. *Nat. Commun.* **7**, 13612 (2016).
31. Zhou, T., Zhang, J. Y., Jiang, H., Žutić, I. & Yang, Z. Q. Giant spin-valley polarization and multiple Hall effect in functionalized bismuth monolayers. *npj Quantum Mater.* **3**, 39 (2018).
32. Chen, M. X. & Weinert, M. Layer k-projection and unfolding electronic bands at interfaces. *Phys. Rev. B* **98**, 245421 (2018).
33. Chen, M. X., Chen, W., Zhang, Z. & Weinert, M. Effects of magnetic dopants in $(Li_{0.8}M_{0.2}OH)$ FeSe (M = Fe, Mn, Co): density functional theory study using a band unfolding technique. *Phys. Rev. B* **96**, 245111 (2017).
34. Chen, M. X. & Weinert, M. Revealing the substrate origin of the linear dispersion of Silicene/Ag(111). *Nano Lett.* **14**, 5189–5193 (2014).
35. Zhai, B. *et al*. Spin-dependent Dirac electrons and valley polarization in the ferromagnetic stanene/CrI₃ van der Waals heterostructure. *Phys. Rev. B* **100**, 195307 (2019).
36. Marzari, N. & Vanderbilt, D. Maximally localized generalized Wannier functions for composite energy bands. *Phys. Rev. B* **56**, 12847 (1997).
37. Souza, I., Marzari, N. & Vanderbilt, D. Maximally localized Wannier functions for entangled energy bands. *Phys. Rev. B* **65**, 035109 (2001).
38. Mostofi, A. A. *et al*. wannier90: A tool for obtaining maximally-localised Wannier functions. *Comput. Phys. Commun.* **178**, 685 (2008).
39. Liang, Q.-F., Yu, R., Zhou, J. & Hu, X. Topological states of non-Dirac electrons on a triangular lattice. *Phys. Rev. B* **93**, 035135 (2016).
40. Xue, Y., Zhang, J. Y., Zhao, B., Wei, X. Y. & Yang, Z. Q. Non-Dirac Chern insulators with large band gaps and spin-polarized edge states. *Nanoscale* **10**, 8569 (2018).
41. Xue, Y. *et al*. Novel Chern insulators with half-metallic edge states. *NPG Asia Mater.* **10**, 467 (2018).
42. Xu, X. H. *et al*. Carrier-induced ferromagnetism in n-type ZnMnAlO and ZnCoAlO thin films at room temperature. *New J. Phys.* **8**, 135 (2006).
43. Momma, K. & Izumi, F. VESTA 3 for three-dimensional visualization of crystal, volumetric and morphology data. *J. Appl. Crystallogr.* **44**, 1272–1276 (2011).
44. Kresse, G. & Furthmüller, J. Efficient iterative schemes for ab initio total-energy calculations using a plane-wave basis set. *Phys. Rev. B* **54**, 11169 (1996).
45. Sun, J., Ruzsinszky, A. & Perdew, J. P. Strongly constrained and appropriately normed semilocal density functional. *Phys. Rev. Lett.* **115**, 036402 (2015).
46. Böker, T. *et al*. Band structure of MoS₂, MoSe₂, and a-MoTe₂: angle-resolved photoelectron spectroscopy and ab initio calculations. *Phys. Rev. B* **64**, 235305 (2001).

Acknowledgements

Author contributions

Xinyuan Wei carried out the first-principles calculations with the assistance of Jiayong Zhang and Bao Zhao. Xinyuan Wei, Zhongqin Yang, and Jiayong Zhang wrote the manuscript. All authors analyzed the results. Zhongqin Yang guided the whole project.

Competing interests

The authors declare no competing interests.

Additional information

Correspondence and requests for materials should be addressed to Z.Y.

Reprints and permissions information is available at www.nature.com/reprints.

Publisher's note Springer Nature remains neutral with regard to jurisdictional claims in published maps and institutional affiliations.